Tunable Wavelength Selectivity of Photonic Metamaterials-based Thermal Devices

Yanpei Tian[a], **Alok Ghanekar**[a], **Xiaojie Liu**[a], **Jie Sheng**[b], **Yi Zheng**[a*]
[a]Department of Mechanical, Industrial and Systems Engineering, University of Rhode Island, Kingston, RI, US 02881
[b]The First Hospital of China Medical University, Shenyang, China 110001

Abstract. Wavelength selective thermal devices have great applications in concentrating solar power systems, high-temperature thermoelectric systems and solar thermophotovoltaics (STPVs). Lack of high-temperature stability and spectrally selective emissivity in different wavelength regions limit their efficiency. In this work, we propose a one-dimensional HfO_2/Al_2O_3-W nanocomposites/W/Al_2O_3/W multilayered photonic structure as potential wavelength selective thermal devices, and theoretically investigate the emission properties of the proposed Mie-resonance metamaterials from visible (VIS) to mid-infrared (MIR) region. HfO_2 thin layer is introduced to serve as an anti-reflection coating film and W layer acts as an IR reflection layer that enhances the absorptivity/emissivity in VIS and near-infrared (NIR) region, while reducing the MIR emission simultaneously. Effects of geometric parameters are discussed, such as different radii and volume fractions of W nanoparticles, the thickness of Al_2O_3-W nanocomposites and HfO_2 thin film. The proposed thermal absorber and emitter exhibit nearly unity absorptance in both VIS and NIR regions, while the emittance approaches zero in the MIR region. The selective absorption/emission window is tunable by varying geometric parameters. The proposed solar thermal devices have great potentials in engineering applications such as STPVs and solar thermoelectric generator (STEG) due to flexibility of geometric parameters and ease of fabrication.

Keywords: Wavelength Selective, Solar Absorber and Emitter, High Temperature, Metamaterials.

*Yi Zheng, zheng@uri.edu

1 Introduction

The increasing energy crisis and global warming enforce us to explore alternative clean energy. Abundant solar energy paves the way to solving the challenging energy demand. Solar thermophotovoltaics (STPVs), which convert sunlight into thermal emission and tune to photons above the photovoltaic (PV) bandgap through a high temperature absorber-emitter, have the potential to act as a promising alternative approach for the existing power generation methods. Schematic of a typical STPV system is represented in Fig.1 (a). STPVs consist of concentrating optics, hot absorber-emitter, PV cell, and heat sink. The concentrating optics transform parallel solar lights into a highly focused light spot that casts on the thermal absorber. The hot absorber is heated up to a high temperature (around 1,300K)[1–3] and it transfers heat to the thermal emitter. Then, the thermal emitter re-emits a certain spectrum of wavelengths matching well with the absorption characteristics of the PV cell.[4] The heat sink enables the operation of the PV cell at low temperatures The selective thermal devices are vital components affecting the efficiency of a STPV system. An ideal solar thermal absorber has two selective spectra of interest, (1) a unity absorptivity in both UV and NIR ranges where almost all of the solar energy is distributed and (2) a zero emissivity in the MIR range where heat loss owing to self-emission is suppressed.[5] It is worth to mention that the absorptivity of an arbitrary body equates its emissivity in a thermodynamic equilibrium according to the Kirchhoff's law of thermal radiation.[6] External quantum efficiency (EQE) of a PV cell is a ratio of the number of converted electron-hole pairs by the solar cell to the number of incident photons. It is related to the generated photon current when a PV cell is shining by incident lights of certain wavelengths.[7] The PV cell only generates a photon current when the energy of an incident photon is higher than the bandgap of semiconductor materials.[8] Furthermore, the efficiency drop caused by waste heat occurs when the wavelength of incident photons is longer than the corresponding wavelength of the bandgap. These photons are transformed into heat to increase the temperature of the PV cell undesirably. Therefore, a perfect thermal emitter exhibits nearly a unity emissivity in the region of high EQE and a zero emissivity in other regions.[9]

Several studies about selective thermal devices focus on photonic crystals,[10,11] doped materials[12,13] and 1-D or 2-D surface grating structures[14–16] to achieve spectrally selective emission properties. Metamaterials-based absorber/emitter is one type of nanostructures that achieve wavelength selectivity through surface phonon and/or plasmon polaritons.[17] Absorption or emission spectra can be re-shaped due to different composite materials, such as alternatively spaced metal-cermet multilayered structure[18,19] and surface grating structures.[8,20] Chirumamilla et al. experimentally investigate the metal-insulator-metal absorber using Al_2O_3-W refractory thin film and show a high absorptance in the range of 650 nm to 1750 nm[18] after thermal annealing for 4 hours at 800°C. Thomas et al. achieve a measured absorptance of 76% at solar thermal wavelengths and approximately 5% emittance at the MIR region using a CaF_2, Cr and *a*Ge multilayered absorber.[19] Lenert et al choose 1-D Si/SiO_2 photonic crystal as a selective thermal emitter in an STPV system at 1,300 K and achieve an overall system efficiency of 3.2%.[21] Aydin et al. demonstrate that a metal-insulator stack with a nanostructured silver film composed of 1-D crossed trapezoidal arrays with an average absorption of 71% over the entire VIS region.[20] Zhao et al. numerically investigate the emissivity of a 2-D W grating structure on top of SiO_2 thin film and show an emissivity over 90% from 300 nm to 2000 nm. The abovementioned structures of exhibiting wavelength selectivity and high-temperature stability can be integrated into STPVs.

All of 1-D or 2-D surface grating metamaterials and photonic crystals rely on micro and nanofabrication techniques, such as nanoscale photolithography and complex etching technologies, which limit scalable engineering applications. Though multilayered thin film structures is relatively feasible, they do not display an ideal property of a nearly unity absorptivity/emissivity across the entire UV-VIS-NIR regions. Mie-resonance metamaterials are another kind of metamaterials that shows selective emission spectra utilizing Mie resonances of doping nanoparticles. Francoeur, Zhao and Wheeler et al. perform theoretical studies of nanoparticle inclusions into matrix materials.[22–24] Ghanekar et al. theoretically investigate the optical properties of nanoparticle embedded thin films and design a high-temperature selective thermal emitter using W nanoparticles embedded SiO_2 matrix film with an opaque W film[1,4] in both far-field and near-field limits. However, the emissivity of all the above structures in the VIS-NIR region is not approaching to unity. There are much improvement of reducing the thermal leakage considering a high emissivity beyond 2 μm. It is desirable to design a highly selective solar thermal device with unity

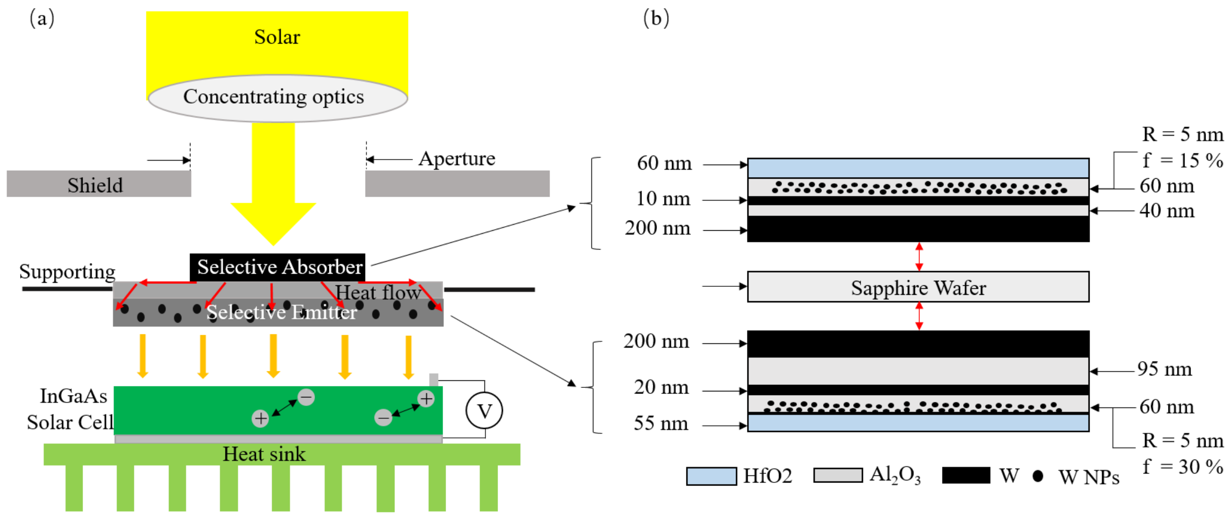

Fig 1 (a) Schematic of a STPV system consisting of concentrating optics, Mie-resonance metamaterial absorber and emitter, an InGaAs solar cell and a heat sink. (b) A proposed structure of thermal absorber and emitter deposited on double sides polished sapphire wafer. The absorber and emitter consist of different thicknesses of Al_2O_3 and W thin films alternately. Layer thickness, starting from the top HfO_2 layer, in the unit of nm, are: [60, **60**, 10, **40**, 200, **4300**, 200, **95**, 20, **60**, 55]. Two Al_2O_3 layers are doped with W nanoparticles of 5 nm radii with a volume fraction of 15% and 30%, respectively.

absorptance/emittance in the UV and NIR regions and zero emittance in the MIR region, which correspond spectrally to the wavelengths that are relevant to solar radiation and high EQE of PV cells .

In this work, we theoretically design photonic metamaterials consisting of multilayered thin film with W nanoparticle inclusions on an opaque W film as a perfect selective solar thermal device. The effective dielectric properties of these materials are investigated over a broad range of VIS-NIR-MIR using Maxwell-Garnett-Mie theory. The investigation of effects of geometric parameters is also conducted, including different radius (R) and volume fraction (VF) of W nanoparticles, the thicknesses of Al_2O_3-W nanocomposites layer and HfO_2 thin film. Perfect solar thermal devices based on Mie-resonance multilayered structure are proposed. Figure1(b) illustrates an example of photonic metamaterials-based selective thermal devices. The solar absorber consists of a 60 nm HfO_2 layer as anti-reflection coating, a 60 nm Al_2O_3 layer doped with W nanoparticles of 5 nm radius, a 10 nm W layer and a 40 nm Al_2O_3 layer on top of a 200 nm W thin film. The W layer acts as an IR reflection layer that reduces the MIR thermal emission. All of these layers are deposited on a double sides polished sapphire wafer. The thermal emitter comprises a similar structure with distinct thickness of each layer and different volume fraction of W nanoparticles as depicted in Fig. 1(b).

2 Theoretical Fundamentals

Considering that the designed solar thermal absorber and emitter are both multilayered thin film structures with nanoparticle inclusions, theoretical calculations of absorptivity and emissivity of multilayered structures are highly desirable. Supposing a structure having N layers media, the generalized reflection coefficient at the interface between region i and region $i + 1$ is given by,[25]

$$\widetilde{R}^{(\mu)}_{i,i+1} = \frac{R^{(\mu)}_{i,i+1} + \widetilde{R}^{(\mu)}_{i+1,i+2} e^{2jk_{i+1,z}(d_{i+1}-d_i)}}{1 + R^{(\mu)}_{i,i+1} \widetilde{R}^{(\mu)}_{i+1,i+2} e^{2jk_{i+1,z}(d_{i+1}-d_i)}} \tag{1}$$

where $R^{(\mu)}_{i,i+1}$ is the Fresnel reflection coefficient at the interface between the layer i and $i+1$, and $\widetilde{R}^{(\mu)}_{i+1,i+2}$ is the generalized reflection coefficient at the interface between the layer $i+1$ and $i+2$, $\mu = s$ (or p) refers to transverse electric (or magnetic) polarization, $z = -d_i$ is the location of the ith interface. $k_{i,z} = \sqrt{\varepsilon_i(\omega)\omega^2/c^2 - k_\rho^2}$ is the normal z-component of the wave vector in medium i wherein $\varepsilon_i(\omega)$ is the relative permittivity of the medium i as a function of angular frequency ω, c is the speed of light in vacuum and k_ρ is the magnitude of the in-plane wave vector. With $\widetilde{R}^{(\mu)}_{N,N+1} = 0$, the above equation provides a recursive relation to calculate the reflection coefficients $\widetilde{R}^{(\mu)}_{i,i+1}$ in all regions. The generalized transmission coefficient for the layered slab is given by[25]

$$\widetilde{T}_{1,N}^{(\mu)} = \prod_{i=1}^{N-1} e^{jk_{iz}(d_i - d_{i-1})} S_{i,i+1}^{(\mu)} \tag{2}$$

The hemispherical emissivity is given by the expression[26]

$$\epsilon(\omega) = \frac{c^2}{\omega^2} \int_0^{\omega/c} dk_\rho k_\rho \sum_{\mu=s,p} (1 - |\widetilde{R}_{h1}^{(\mu)}|^2 - |\widetilde{T}_{h1}^{(\mu)}|^2) \tag{3}$$

where $\widetilde{R}_h^{(\mu)}$ and $\widetilde{T}_h^{(\mu)}$ are the polarization dependent effective reflection and transmission coefficients which can be determined using Eqs.1 and 2.

The dielectric functions of materials used in this paper (HfO_2, Al_2O_3, W thin film and W nanoparticles) are related to refractive index as $\sqrt{\varepsilon} = n + j\kappa$, where n and κ are real and imaginary parts of refractive index. The effective dielectric function of the Mie-resonance metamaterials is expressed as Clausius-Mossotti equation.[27,28]

$$\varepsilon_{eff} = \varepsilon_m \left(\frac{R^3 + 2\alpha_R VF}{R^3 - \alpha_R VF} \right) \tag{4}$$

where ε_m is the dielectric function of the matrix, α_R is the electric dipole polarizability, R and VF are the radius and volume fraction of nanoparticles respectively. Mie theory is an useful method of considering the size of doping nanoparticles. Maxwell-Garnett formula using Mie theory[29] is employed to express the electric dipole polarizability,

$$\alpha_R = \frac{3jc^3}{2\omega^3 \varepsilon_m^{3/2}} a_{1,R} \tag{5}$$

where $a_{1,R}$ is the first electric Mie coefficient given by

$$a_{1,R} = \frac{\sqrt{\varepsilon_{np}}\psi_1(x_{np})\psi_1'(x_m) - \sqrt{\varepsilon_m}\psi_1(x_m)\psi_1'(x_{np})}{\sqrt{\varepsilon_{np}}\psi_1(x_{np})\xi_1'(x_m) - \sqrt{\varepsilon_m}\xi_1(x_m)\psi_1'(x_{np})} \tag{6}$$

where ψ_1 and ξ_1 are Riccati-Bessel functions of the first order given by $\psi_1(x) = xj_1(x)$ and $\xi_1(x) = xh_1^{(1)}(x)$ where j_1 and $h_1^{(1)}$ are first order spherical Bessel functions and spherical Hankel functions of the first kind, respectively. Here, '′' indicates the first derivative. $x_m = \omega r\sqrt{\varepsilon_m}/c$ and $x_{np} = \omega r\sqrt{\varepsilon_{np}}/c$ are the size parameters of the matrix and the nanoparticles, respectively; ε_{np} being the dielectric function of nanoparticles.

Dielectric functions of abovementioned materials are given in these literature.[30–32] Since all the melting temperatures of the materials considered in this paper are over 2,300K and the operating temperature (1,300K) is much less than the melting point, the dielectric properties of these materials are assumed to be constant. Each layer of the designed structure is uniform, including the nanoparticles embedded thin film, so it is reasonable that each layer can be approximated as a homogeneous layer and its effective dielectric function can be evaluated and utilized in theoretical calculations. It is also worth to notice that the size (10 nm) of W nanoparticles is much smaller than the wavelengths of interest (λ = 0.3 μm – 20 μm), so the Maxwell-Garnett-Mie theory is appropriate in this study.[33]

3 Calculation Results and Discussion

3.1 Refractive Indices and Penetration Depth of Nanoparticle Inclusions

Figure 2 elucidate the effects of W nanoparticle inclusions on the refractive indices of Al_2O_3 matrix in the wavelength range from 0.3 μm to 5μm, aiming to illustrate the physical mechanisms responsible for the enhanced emissivity/absorptivity that gives rise to high emissivity/absorptivity in both VIS and NIR regions. Figure 2 shows that the real part of refractive index ($n \approx 1.7$) of the pure Al_2O_3 is nearly constant and the imaginary part ($\kappa \approx 0.02$) is nearly negligible. The introduced W nanoparticles increase both the real and imaginary parts of refractive index of Al_2O_3, when the VF of W nanoparticles increases. It can be seen that both the real and imaginary parts of refractive index of Al_2O_3-W nanocomposites also increase (see the curve of Al_2O_3 thin film embedded with a VF of 15% and 30% W nanoparticles). Since the effective refractive index of nanocomposites relies on different components, and the inclusion of W nanoparticles (R = 10 nm) is much smaller than the investigated wavelengths (λ = 0.3μm – 5μm) that causes the Mie-scattering of the incidence, the change of refractive index of Al_2O_3-W nanocomposites results from the mixture of different constituents and wave scattering of W nanoparticles. Figure. 2(a) shows that the real part (n) of refractive index of Al_2O_3-W nanocomposites goes up from 0.3 μm to 1.8 μm and it has a peak around 1.8 μm, then declines. Simultaneously, Figure 2(b) gives that the imaginary part (κ) of Al_2O_3-W nanocomposites slowly decreases from 0.3 μm to 1.8 μm and suddenly drops around 1.8 μm. However, the real part of refractive index of W keeps at a relatively high value (above 3) from 0.3 μm to 1.8 μm, then falls down to valley around 2.2 μm and then increases, and its imaginary part rises continuously, which does not correspond to the trend of the change in its real part of nanocomposites for both VFs of 15% and 30%. It can be concluded that when the wavelength of the incident light is small, the inclusion of W nanoparticles causes the Mie-scattering; when the wavelength of the incident light is large, no scattering is caused by W nanoparticles. For this reason, the real parts of the Al_2O_3-W nanocomposites increase in the region of 0.3 μm to 1.8 μm, while its imaginary parts decline at a slow pace. Otherwise, they would have drop sharply. When the wavelength of incident light is greater than 1.8 μm, both the

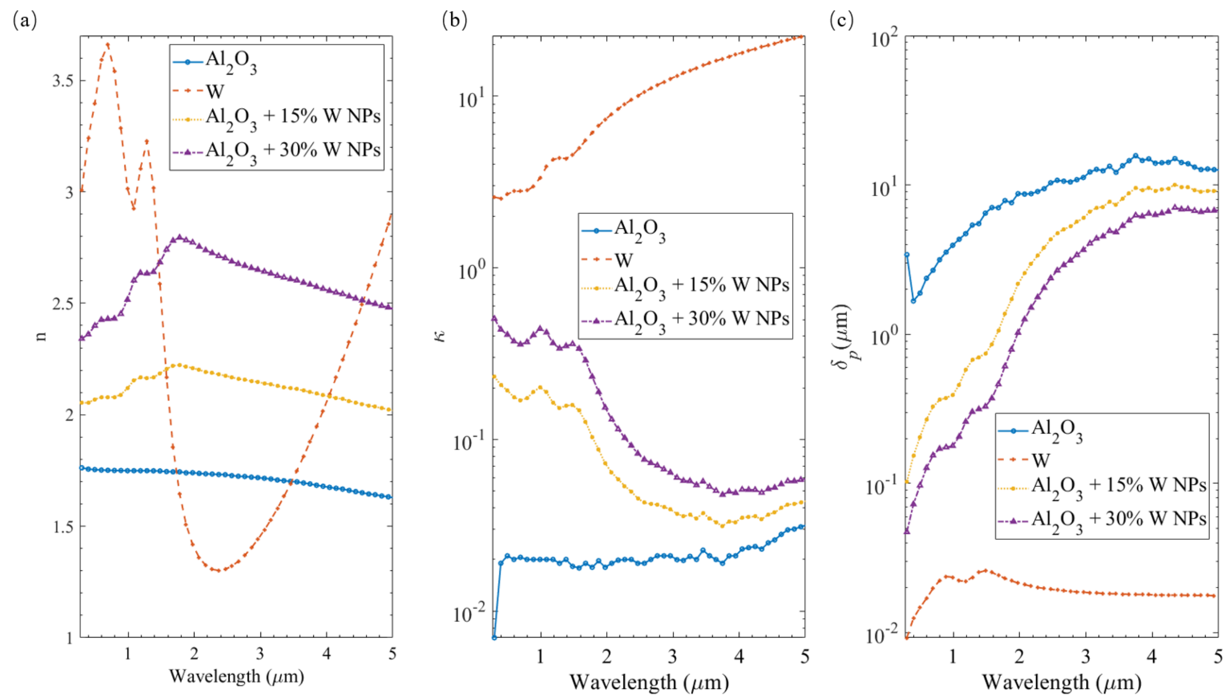

Fig 2 Refractive indices and penetration depths of W, Al_2O_3 and Al_2O_3 doped with W nanoparticles of 5 nm radius and volume fraction of 15% and 30%, respectively. (a) Real part of refractive indices. (b) Imaginary part of refractive indices. (c) The penetration depth from λ = 0.3 μm to 5 μm.

real and imaginary parts decrease quickly.

Figure 2(c) shows the penetration depths of pure Al_2O_3, W, and Al_2O_3-W nanocomposites of two different VFs. By introducing W nanoparticles, the penetration depth of Al_2O_3-W nanocomposites is smaller than the pure Al_2O_3 because of the scattering effect of W nanoparticles. The increasing VF of W nanoparticles gives rise to the decrease in the penetration depth of Al_2O_3-W nanocomposites. Figure 2(c) also shows that the maximum penetration depth of pure W is around 25 nm, which ensures all the incident lights are reflected back by the bottom W layer and the structure can be treated as opaque.

3.2 Effect of Geometric Parameters

We investigate the geometric effects on the emissivity/absorptivity of designed Mie-resonance metamaterials-based solar thermal absorber/emitter at normal incidence, in order to clarify a dom-

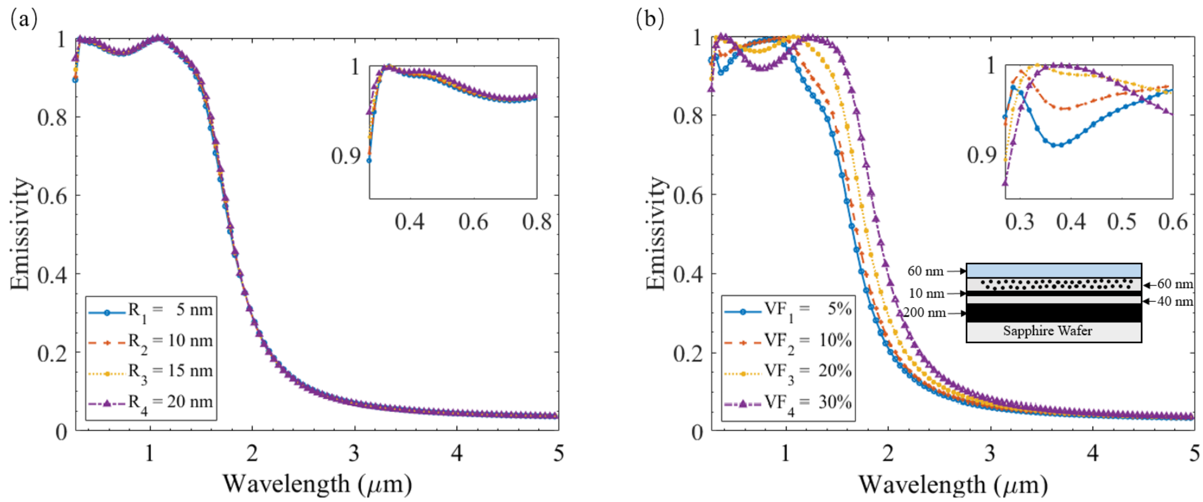

Fig 3 Emissivity/absorptivity spectra as a function of (a) the size of W nanoparticles with radius of 5 nm, 10 nm, 15 nm and 20 nm, respectively, embedded in Al_2O_3 layer, (b) the volume fraction of W nanoparticles of 5%, 10 %, 20 % and 30 %, respectively, embedded in Al_2O_3 layer. The investigated structure is shown in the inset of Fig.3(b). The top right insets are both the zoom-in wavelength regions from λ = 0.3 μm to 0.8 μm.

inated mechanism for the selective emissivity/absorptivity and to get an optimized geometric parameters for the designed structure. The effects of size and volume fraction of W nanoparticles, the thickness of Al_2O_3-W nanocomposites layer and the thickness of anti-reflection HfO_2 layer are set to the base geometric parameters shown in the insets of Fig. 3(b) and Fig. 4(b). Other geometric effects are fixed to the base geometric parameters when one of the investigated parameters varies in our calculations. The incident angle is fixed at 0°. Figures 3 and 4 show how the emissivity/absorptivity varies with various geometric parameters in the wavelength region from 0.3 μm to 5 μm, where most of the solar energy is distributed.

Figure 3(a) shows that there are two peaks with an enhanced emissivity significantly up to about 1 at around λ = 0.35 μm and λ = 1.15 μm corresponding to the two peaks of real part of pure W, as shown in the Fig. 2(a). With the radius of W nanoparticles increasing from 5 nm to 20 nm and the VF of W nanoparticles is fixed at 20%, the two peaks remain almost un-shifted and there is unnoticeable fluctuations of the magnitude of these peaks, which indicates that the peak wavelength and magnitude has much less dependence on the size of the W nanoparticles. It is reasonable that the maximum diameter of W nanoparticles is 40 nm which is quite smaller compared to the minimum investigated wavelength (300 nm), so the size of the W nanoparticles shows little effect on the emissivity performance when the W nanoparticles have relatively small radii. For the two emissivity peaks, it is owing to the excitation of surface plasmon polaritons (SPPs) of W. Such similar emissivity peaks have been discovered at short wavelengths in the 2-D metamaterials-based TPV emitters,[8] which is attributed to the excitation of SPPs for metallic W.

When the radius of the W nanoparticles is set to 5 nm and the VF varies, as shown in Fig. 3(b), the overall emissivity raises together with an increment of VF of W nanoparticles from 5% to 20%, however, it drops after the VF approaches 30%. The first set of emissivity peaks emerging at around 0.35 μm increases and shifts to a longer wavelength corresponding to the increment of VF of W nanoparticles. It can also be observed that the second set of emissivity peaks shifts to a longer wavelength from 1.0μm to 1.3 μm with an increasing VF. Since the W support SPPs, the right-shifts of two peaks presented here can be attributed to the excitation of SPPs. Ghanekar et al.[34] discuss explicitly on the behavior of SPPs of the metal (Au) nanoparticles embedded in SiC matrix that is similar to the structures discussed here.

As shown in Fig. 4(a), the thickness of the top Al_2O_3-W nanocomposites layer yields similar effect as the VF of W nanoparticles on the emissivity of Mie-resonance solar thermal absorber/emitter at normal incidence. When the thickness of Al_2O_3-W nanocomposites changes from 40 nm to 240 nm, the first set of emissivity peaks emerging at around 0.4 μm do not show clear preferred direction of the shifts. While the position of the second set of emissivity peaks that appear at over 1.2 μm and shifts obviously to the right and the magnitude of these peaks drops abruptly when the thickness of the top Al_2O_3-W nanocomposites layer increase to 150 nm. Similarly, the

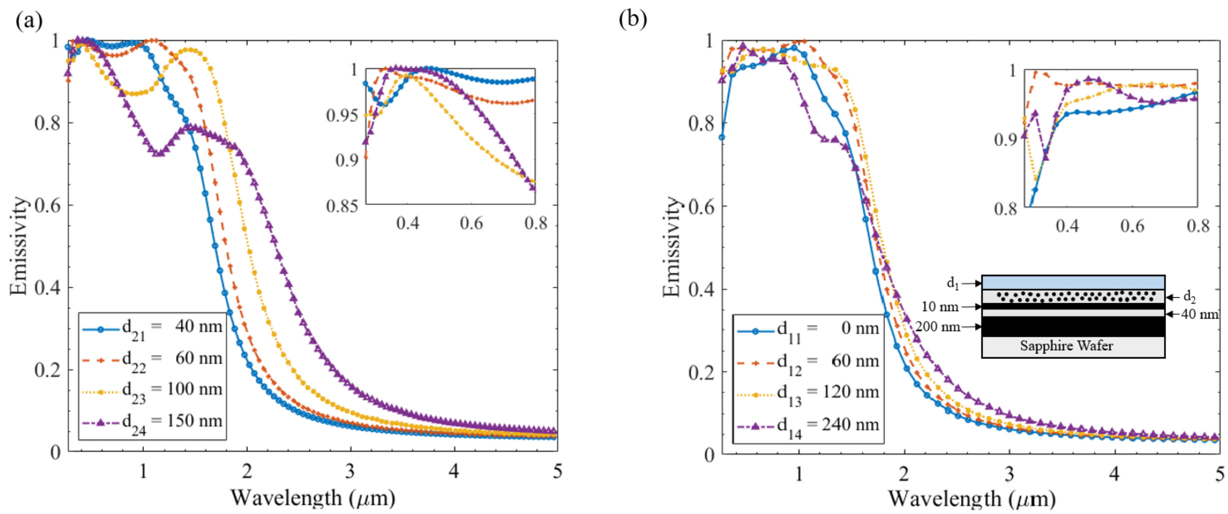

Fig 4 Emissivity/absorptivity spectra as a function of (a) thickness of the top Al_2O_3-W nanocomposites layer of 40 nm, 60 nm, 120 nm and 240 nm, respectively, (b) thickness of the anti-reflection HfO_2 coating layer of 0 nm, 60 nm, 120 nm and 240 nm, respectively. The base investigated structure is as shown in the inset of Fig.4(b). The top right insets are both the zoom-in wavelength regions from λ = 0.3 μm to 0.8 μm.

average emissivity of solar thermal absorber/emitter drops with the increment of the thickness of the top Al_2O_3-W nanocomposites layer. As a result, a relatively high and broad emissivity band from 0.3 μm to 1.5 μm can be achieved with a thickness around 60 nm.

Figure 4(b) shows the effect of the thickness of the anti-reflection HfO_2 layer on the emissivity of solar thermal devices at normal incidence. It can been seen that the average emissivity of a broad spectral band from 0.3 μm to 1.6 μm is enhanced when the thickness of the HfO_2 layer is 60 nm compared to a structure without an HfO_2 layer. The average emissivity from 0.3 μm to 1.6 μm decreases when the thickness of HfO_2 layer is thicker at 120 nm or 240 nm. On the other side, when the thickness of HfO_2 layer varies from 0 nm to 240 nm, the emissivity of solar thermal devices increases for long wavelengths ($\lambda > 2$ μm). Considering the overall performance, the HfO_2 layer with a thickness of 60 nm gives the best performance.

Conclusively, the emissivity of the Mie-resonance solar thermal absorber/emitter strongly depends on the geometric parameters. It can be seen clearly that there exist two emissivity peaks due to the excitation of SPPs modes and a broad band with an enhanced emissivity in both the VIS and NIR regions. Meanwhile, the locations and magnitudes of peak emissivity wavelengths depend significantly on the size and VF of W nanoparticle inclusions and the thickness of the Al_2O_3-W nanocomposites layer. The introduction of HfO_2 layer will improve the overall performance of the solar thermal absorber/emitter, and it will enhance the emissivity up to 1 in the short wavelength region (from 0.3 μm to 1.6 μm) and reduce the emissivity down to 0 in the long region ($\lambda > 1.8$ μm).

3.3 Optimized Structures

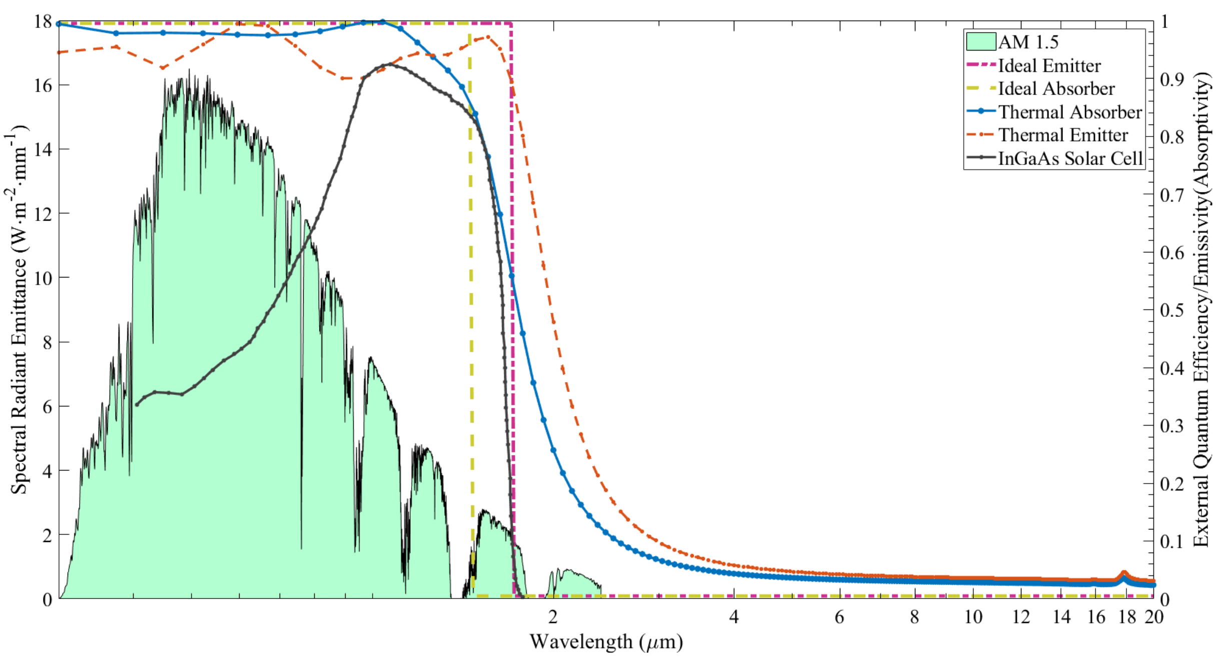

Fig 5 Emission spectra of an optimized solar thermal absorber and emitter, and an ideal selective thermal absorber and emitter. The incident solar spectrum (AM 1.5) and the EQE of InGaAs PV cell are shown for reference.

According to the geometric effects on the emissivity of solar thermal device, optimized structures of solar thermal absorber/emitter are shown in Fig.1(b). The solar thermal absorber presented here is applicable to the STPV applications under high concentration ratio solar lights at AM 1.5 conditions. As shown in Fig. 5, the ideal solar absorber has a up to 1 emissivity from 0.3 μm to 1.6 μm where most of the solar energy is distributed, while its emissivity reduces down to 0.1 beyond 2.3 μm. The emissivity curve of the designed solar absorber structure perfectly matches to an ideal thermal absorber, giving rise to the absorber receives as much solar energy as possible and reducing its self-emitting at a high temperature (~1,300K). The thermal emitter, as shown in Fig. 1(b), is suitable for a STPV system with an InGaAs based PV cell. The EQE curve of the InGaAs PV cell is shown in Fig. 5. The efficiency of the InGaAs PV cell is high when the wavelength of incident photons falls in the region between 0.3 μm and 1.8 μm. The proposed thermal emitter exhibits a high emissivity (> 0.92) in the wavelength range from 0.3 μm to 1.8 μm, and an extremely low emissivity (< 0.1) beyond 2.9 μm. Both the solar thermal absorber and emitter have a near zero emissivity beyond 4 μm. The close match between the emission spectrum and the EQE curve of PV cell ensures a high conversion efficiency and minimizes the thermal leakage of low energy photons. Since the melting points of the selected materials (Al_2O_3 and W) are over $2,300$K and their linear temperature expansion coefficients of Al_2O_3 (8.1×10^{-6}m/(m·K)) and W (4.5×10^{-6}m/(m·K)) are at the same order of magnitude, the solar absorber and emitter both have a high temperature stability that ensures a high efficiency of the STPV system at a high temperature. In addition, fabrication of the multilayered solar thermal absorber and emitter is relatively simple, in comparison to the 1-D or 2-D surface grating structures which require nanoscale photolithography and complex dry or wet etching. The deposition of Al_2O_3, W and Al_2O_3-W nanocomposites thin films can be achieved by Magnetron Sputtering Technology.[35] As refractory materials such as tungsten and Al_2O_3 have been chosen to be materials of thermal emitter, it is reasonable that the proposed structures of solar thermal absorber and emitter have a great potential to be an scalable-manufactured engineering metamaterials.

4 Conclusions

In this work, we have theoretically designed a selective thermal device made of Mie-resonance metamaterials consisting of multilayered structures with nanoparticle inclusions. High absorptivity/emissivity in the visible and near-infrared regions and low emittance in the mid-infrared region can be attained through such a structure. The effects of geometric parameters on the optical properties of the solar thermal absorber/emitter have been elucidated in details. The absorptivity/emissivity is enhanced to be unity as desired with optimized geometric parameters such as size and volume fraction of W nanoparticles, thickness of Al_2O_3-W nanocomposites layer, and the thickness of anti-reflection HfO_2 layer. The spectral absorptivity of the proposed solar thermal absorber is up-to-unity in the wavelength range from 0.3 μm to 1.6 μm, while its spectral emissivity is lower than 0.1 from 2.3 μm to 20 μm. Moreover, the solar thermal emitter has an emissivity over 0.92 from 0.3 μm to 1.8 μm, while remaining as low as 0.1 from 2.9 μm to 20 μm. Design of the proposed metamaterials-based solar absorber and emitter will benefit the performance of STPV systems and can also be applied to solar energy harvesting and traditional TPV systems.

5 Acknowledgements

This project was supported in part by a National Science Foundation through grant number 1655221, Institutional Development Award (IDeA) Network for Biomedical Research Excellence from the National Institute of General Medical Sciences of the National Institutes of Health through grant number P20GM103430, and National Aeronautics and Space Administration through grant number NNX15AK52A.

References

1 A. Ghanekar, Y. Tian, S. Zhang, *et al.*, "Mie-metamaterials-based thermal emitter for near-field thermophotovoltaic systems," *Materials* **10**(8), 885 (2017).

2 Y. Tian, A. Ghanekar, M. Ricci, *et al.*, "A review of tunable wavelength selectivity of metamaterials in near-field and far-field radiative thermal transport," *Materials* **11**(5), 862 (2018).

3 A. Ghanekar, M. Sun, Z. Zhang, *et al.*, "Optimal design of wavelength selective thermal emitter for thermophotovoltaic applications," *Journal of thermal science and engineering applications* **10**(1), 011004 (2018).

4 A. Ghanekar, L. Lin, and Y. Zheng, "Novel and efficient mie-metamaterial thermal emitter for thermophotovoltaic systems," *Optics express* **24**(10), A868–A877 (2016).

5 N. P. Sergeant, O. Pincon, M. Agrawal, *et al.*, "Design of wide-angle solar-selective absorbers using aperiodic metal-dielectric stacks," *Optics express* **17**(25), 22800–22812 (2009).

6 Z. Zhang, *Nano/Microscale Heat Transfer*, McGraw-Hill, New York (2007).

7 W. R. Chan, P. Bermel, R. C. Pilawa-Podgurski, *et al.*, "Toward high-energy-density, high-efficiency, and moderate-temperature chip-scale thermophotovoltaics," *Proceedings of the National Academy of Sciences* **110**(14), 5309–5314 (2013).

8 B. Zhao, L. Wang, Y. Shuai, *et al.*, "Thermophotovoltaic emitters based on a two-dimensional grating/thin-film nanostructure," *International Journal of Heat and Mass Transfer* **67**, 637–645 (2013).

9 Y. Zheng, "Thermal radiative wavelength selectivity of nanostructured layered media," in *Nanoscaled Films and Layers*, InTech (2017).

10 P. Nagpal, S. E. Han, A. Stein, *et al.*, "Efficient low-temperature thermophotovoltaic emitters from metallic photonic crystals," *Nano letters* **8**(10), 3238–3243 (2008).

11 K. A. Arpin, M. D. Losego, A. N. Cloud, *et al.*, "Three-dimensional self-assembled photonic crystals with high temperature stability for thermal emission modification," *Nature communications* **4** (2013).

12 F. Cao, D. Kraemer, L. Tang, *et al.*, "A high-performance spectrally-selective solar absorber based on a yttria-stabilized zirconia cermet with high-temperature stability," *Energy & Environmental Science* **8**(10), 3040–3048 (2015).

13 F. Cao, L. Tang, Y. Li, *et al.*, "A high-temperature stable spectrally-selective solar absorber based on cermet of titanium nitride in sio 2 deposited on lanthanum aluminate," *Solar Energy Materials and Solar Cells* **160**, 12–17 (2017).

14 H. Wang and L. Wang, "Perfect selective metamaterial solar absorbers," *Optics express* **21**(106), A1078–A1093 (2013).

15 A. Moreau, C. Ciraci, J. J. Mock, *et al.*, "Controlled-reflectance surfaces with film-coupled colloidal nanoantennas," *Nature* **492**(7427), 86 (2012).

16 M. G. Nielsen, A. Pors, O. Albrektsen, *et al.*, "Efficient absorption of visible radiation by gap plasmon resonators," *Optics express* **20**(12), 13311–13319 (2012).

17 A. Ghanekar, Y. Tian, and Y. Zheng, "Photonic metamaterials: Controlling nanoscale radiative thermal transport," (2018).

18 M. Chirumamilla, A. S. Roberts, F. Ding, *et al.*, "Multilayer tungsten-alumina-based broadband light absorbers for high-temperature applications," *Optical Materials Express* **6**(8), 2704–2714 (2016).

19 N. H. Thomas, Z. Chen, S. Fan, *et al.*, "Semiconductor-based multilayer selective solar absorber for unconcentrated solar thermal energy conversion," *Scientific reports* **7**(1), 5362 (2017).

20 K. Aydin, V. E. Ferry, R. M. Briggs, *et al.*, "Broadband polarization-independent resonant light absorption using ultrathin plasmonic super absorbers," *Nature communications* **2**, 517 (2011).

21 A. Lenert, D. M. Bierman, Y. Nam, *et al.*, "A nanophotonic solar thermophotovoltaic device," *Nature nanotechnology* **9**(2), 126–130 (2014).

22 M. Francoeur, S. Basu, and S. J. Petersen, "Electric and magnetic surface polariton mediated near-field radiative heat transfer between metamaterials made of silicon carbide particles," *Optics express* **19**(20), 18774–18788 (2011).

23 Q. Zhao, J. Zhou, F. Zhang, *et al.*, "Mie resonance-based dielectric metamaterials," *Materials Today* **12**(12), 60–69 (2009).

24 M. S. Wheeler, J. S. Aitchison, and M. Mojahedi, "Three-dimensional array of dielectric spheres with an isotropic negative permeability at infrared frequencies," *Physical Review B* **72**(19), 193103 (2005).

25 W. C. Chew and W. C. Chew, *Waves and fields in inhomogeneous media*, vol. 522, IEEE press New York (1995).

26 A. Ghanekar, L. Lin, J. Su, *et al.*, "Role of nanoparticles in wavelength selectivity of multilayered structures in the far-field and near-field regimes," *Optics Express* **23**(19), A1129–A1139 (2015).

27 V. Myroshnychenko, J. Rodríguez-Fernández, I. Pastoriza-Santos, *et al.*, "Modelling the optical response of gold nanoparticles," *Chemical Society Reviews* **37**(9), 1792–1805 (2008).

28 U. Kreibig and M. Vollmer, *Optical properties of metal clusters*, vol. 25, Springer Berlin (1995).

29 W. T. Doyle, "Optical properties of a suspension of metal spheres," *Physical review B* **39**(14), 9852 (1989).

30 D. L. Wood, K. Nassau, T. Kometani, *et al.*, "Optical properties of cubic hafnia stabilized with yttria," *Applied optics* **29**(4), 604–607 (1990).

31 M. R. Querry, "Optical constants," tech. rep., MISSOURI UNIV-KANSAS CITY (1985).

32 A. D. Rakić, A. B. Djurišić, J. M. Elazar, *et al.*, "Optical properties of metallic films for vertical-cavity optoelectronic devices," *Applied optics* **37**(22), 5271–5283 (1998).

33 M. S. Wheeler, *A scattering-based approach to the design, analysis, and experimental verification of magnetic metamaterials made from dielectrics*. PhD thesis (2010).

34 A. Ghanekar, L. Lin, J. Su, *et al.*, "Role of nanoparticles in wavelength selectivity of multilayered structures in the far-field and near-field regimes," *Optics express* **23**(19), A1129–A1139 (2015).

35 M. Austgen, D. Koehl, P. Zalden, *et al.*, "Sputter yield amplification by tungsten doping of al2o3 employing reactive serial co-sputtering: process characteristics and resulting film properties," *Journal of Physics D: Applied Physics* **44**(34), 345501 (2011).